

Collision Induced Relaxations within the Antiprotonic Helium Hyperfine Structure

T Pask¹, D Barna^{2,3}, A Dax², S Friedreich¹, R S Hayano²,
M Hori^{2,4}, D Horváth^{3,5}, B Juhász¹, C Malbrunot^{1‡},
O Massiczek¹, N Ono², A Sótér³ and E Widmann¹

¹ Stefan Meyer Institute for Subatomic Physics, Austrian Academy of Sciences, Boltzmanngasse 3, A-1090 Vienna, Austria.

E-mail: thomas.pask@cern.ch

² Department of Physics, University of Tokyo, 7-3-1 Hongo, Bunkyo-ku, Tokyo 113-0033, Japan

³ KFKI Research Institute for Particle and Nuclear Physics, H-1525 Budapest, PO Box 49, Hungary

⁴ Max-Planck-Institut für Quantenoptik, Hans-Kopfermann-Strasse 1, D-85748 Garching, Germany.

⁵ Institute of Nuclear Research of the Hungarian Academy of Sciences, H-4001 Debrecen, PO Box 51, Hungary

Abstract. We report the first measurements of the inelastic spin exchange collision rate between the Hyperfine (HF) levels of antiprotonic helium ($\bar{p}\text{He}^+$). We measure the time dependent evolution of the (37, 35) substates to obtain an inelastic collision rate which qualitatively agrees with recent theoretical calculations. We evaluate these results by using the obtained rate as a parameter in a rigorous simulation which we then compare to previously measured data. We find that our measurement slightly underestimates the collision rate and therefore conclude that the actual value most probably falls within the upper, rather than lower, limit of the error.

PACS numbers: 36.10.-k, 32.10.Fn, 33.40.+f

Submitted to: *J. Phys. B: At. Mol. Opt. Phys.*

‡ Present address: TRIUMF, 4004 Wesbrook Mall, Vancouver, BC, V6T 2A3, Canada.

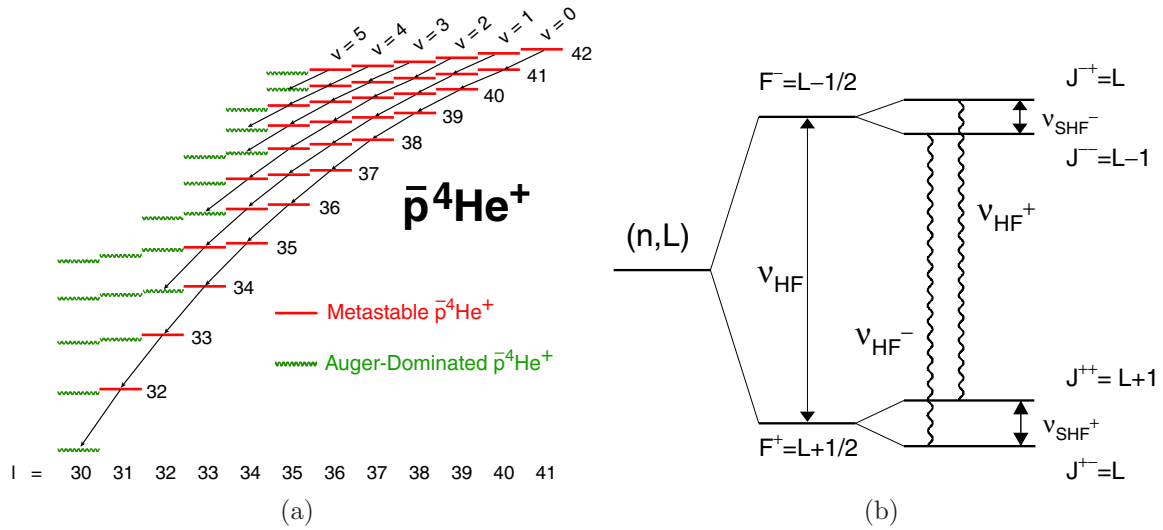


Figure 1: (a) Level diagram of $\bar{p}^4\text{He}^+$ where the arrows indicate the radiative cascade towards the nucleus. (b) Hyperfine splitting of an (n, l) state of $\bar{p}^4\text{He}^+$. The wavy lines denote allowed M1 transitions that can be induced by an oscillating magnetic field. From [1].

1. Introduction

Antiprotonic helium $\bar{p}\text{He}^+$ is formed when an antiproton \bar{p} interacts with a helium atom at or below the ionization energy (~ 25 eV) [2]. The \bar{p} can become captured so that it precesses around the helium nucleus He^{++} [1, 3, 4]. When this happens, one of the electrons e^- is ejected. Because of its mass, the \bar{p} is most likely to occupy an orbit with principle quantum number $n = n_0 \equiv \sqrt{M^*/m_e} \sim 38$ [5], where M^* is the reduced mass of the antiproton-helium nucleus system and m_e is the electron mass. It precesses in a semi-classical orbit while the electron remains in a $1s$ quantum mechanical cloud.

Because of their overlap with the nucleus, the majority of captured antiprotons annihilate within picoseconds with one of the nucleons in the He^{++} nucleus [4]. However, approximately 3% occupy metastable states, so called circular states in the region of $n = 32-40$ and vibrational quantum number $v = 0-3$ (where $v = n - l - 1$ and l is the angular momentum quantum number). Since the neutral system retains one electron, it is protected from external atoms by the Pauli exclusion principle [4]. Additionally, the presence of the electron removes the l degeneracy for the same n , therefore protecting it against Stark mixing. The Auger decay of the remaining electron is suppressed by the large ionization energy compared to the $n \rightarrow n - 1$ level spacing of ~ 2 eV. Thus only one decay channel remains and the antiprotons in these states undergo a radiative cascade through $(n, l) \rightarrow (n - 1, l - 1)$ states, each with lifetimes in the order $\sim 1.5 \mu\text{s}$, see figure 1a.

A *hyperfine (HF)* splitting [4], caused by the interaction of the e^- spin S_e with the \bar{p} orbital angular momentum L , results in a doublet structure of the order $\nu_{\text{HF}} = 10-$

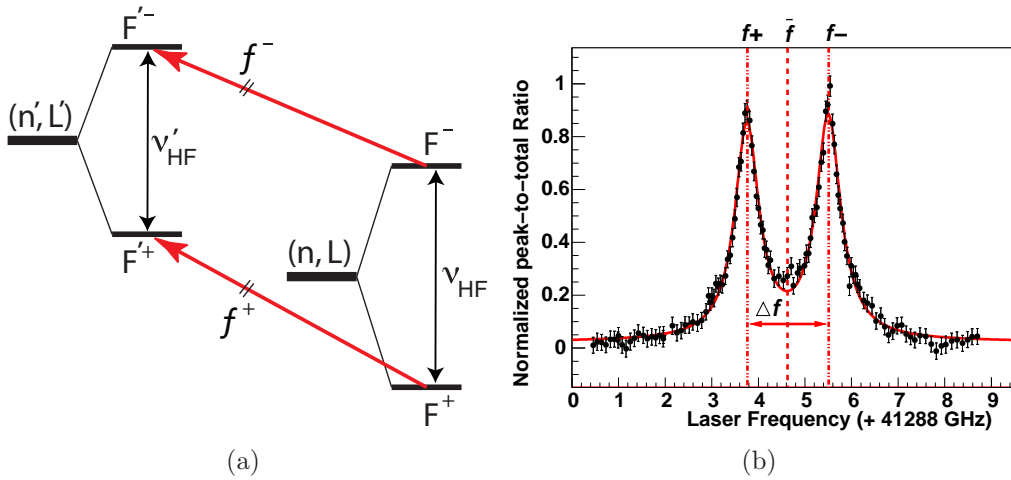


Figure 2: (a) Schematic view of the primary level splitting of $\bar{p}\text{He}^+$ for the unfavoured electric dipole transitions. The state drawn on the right is the radiative decay dominated parent (n, L) , and state on the left is the Auger decay dominated daughter (n', L') . The laser transitions, from the parent to the daughter doublets, are indicated by the arrows f^+ and f^- . (b) Laser resonance profile of the $(n, l) = (37, 35)$ to $(38, 34)$ transition showing the f^+ and f^- transitions, from [7]

15 GHz. A further splitting of each HF state results in a *superhyperfine* (SHF) structure ($\nu_{\text{SHF}} = 150\text{-}300$ MHz), caused by the interaction of the \bar{p} spin $S_{\bar{p}}$ with $F = L + S_e$. There exists therefore a quadruplet substructure for each (n, l) state as shown in figure 1b. The theoretical framework for the level splitting has been developed by Bakalov and Korobov [6].

The HF doublet is described by the quantum number $\vec{F} = \vec{L} + \vec{S}_e$ with components $F^+ = L + \frac{1}{2}$ and $F^- = L - \frac{1}{2}$. The SHF quadruplet is described by $\vec{J} = \vec{F} + \vec{S}_{\bar{p}}$ with components $J^{-+} = F^- + \frac{1}{2}$, $J^{--} = F^- - \frac{1}{2}$, $J^{++} = F^+ + \frac{1}{2}$ and $J^{+-} = F^+ - \frac{1}{2}$. Between these sub states an electron spin flip can be induced by two M1 transitions ν_{HF}^+ and ν_{HF}^- (see figure 1b):

$$\nu_{\text{HF}}^+ : \quad J^{++} = F^+ + \frac{1}{2} = L + 1 \leftrightarrow J^{-+} = F^- + \frac{1}{2} = L, \quad (1a)$$

$$\nu_{\text{HF}}^- : \quad J^{+-} = F^+ - \frac{1}{2} = L \quad \leftrightarrow \quad J^{--} = F^- - \frac{1}{2} = L - 1. \quad (1b)$$

Electric dipole transitions (E1) between different levels of the cascade can be induced with resonant laser light [8–11]. There are two types: favoured, $\Delta v = 0$; $(n, l) \rightarrow (n - 1, l - 1)$, and unfavoured, $\Delta v = 2$; $(n, l) \rightarrow (n + 1, l - 1)$ [4]. The dipole moment of the unfavoured transitions is an order of magnitude smaller than that of the favoured. To the first order, atoms occupying the F^- doublet of the radiative decay dominated state are transferred to the F'^- doublet of the Auger dominated state, while those occupying F^+ are transferred to F'^+ , shown in figure 2a. These transitions are labelled f^+ and f^- respectively and the difference between them Δf . The unfavoured

transitions have $\Delta f = 1.5 - 1.8$ GHz, while the favoured have $\Delta f \leq 0.5$ GHz. The Doppler broadening at the target temperature is $\sim 0.3 - 0.5$ GHz, therefore only the unfavoured HF laser transitions can be well resolved, see figure 2b.

2. Motivation and Method

A precise measurement of the $\bar{p}\text{He}^+$ HF splitting [7, 12, 13] is of great importance for rigorously testing three-body quantum electrodynamic (QED) calculations [6, 14–16], leading to a determination of the antiproton spin magnetic moment and a test of *CPT* invariance [17]. For an understanding of the collision processes between $\bar{p}\text{He}^+$ atoms and the He atoms of the medium, a comparison between experiment and theory can be equally useful. Both the elastic Γ_e and inelastic Γ_i collision rates can have significant systematic effects on experimental results. Elastic collisions contribute to a shift and a broadening $\Delta - i\Gamma_e$, while inelastic collisions result in a spin exchange, therefore a change of state.

A clear understanding of the collision processes was essential for the interpretation of the E1 spectral lines [18], a similar study has been performed for the M1 transitions. To measure $\Delta - i\Gamma_e$, microwave resonant profiles were scanned at various target gas densities. The line width is limited by the Fourier transform of the microwave pulse length but observation of a larger width would be evidence of a collisional broadening. Likewise a density dependent change in the transition frequencies would be evidence of a collisional shift.

The results of elastic collisional studies have been presented in previous publications [7, 19] and indicate that Γ_e is small because the dominating broadening effect is found to be from the Fourier transform of the microwave pulse length. Korenman predicts that $\Gamma_e \sim 2.5\Gamma_i$ [20] which means that if Γ_e is smaller than first predicted then so must Γ_i .

The inelastic collision rate was determined by measuring the time dependence of the F^+ population. Two narrow-band lasers were tuned to the f^+ transition between the radiative decay dominated parent state $(n, L) = (37, 35)$ and the Auger decay dominated daughter state $(38, 34)$ shown in figure 2. The second was delayed by a time $T = 50 - 2000$ ns from the first.

The \bar{p} annihilation products were detected with Cherenkov counters as a function of time. The metastable tail, where the radiative decay dominated states cascade towards the nucleus, was recorded as background. Because of its short lifetime (~ 10 ns), the laser resonant transfer to an Auger dominated decay state results in a sharp peak in annihilations events which stands out against the background, shown in figure 3. The ratio between this peak area to the area under the entire spectrum (peak-to-total) is proportional to the population transferred with the laser. The peak-to-total of the first and second laser annihilation peaks are represented by r_1 and r_2 , respectively.

The experiment was performed in two different modes: 1) where both lasers were fired, $f^+ - f^+$ and 2) where only the second laser was fired, $0 - f^+$, both of which are shown

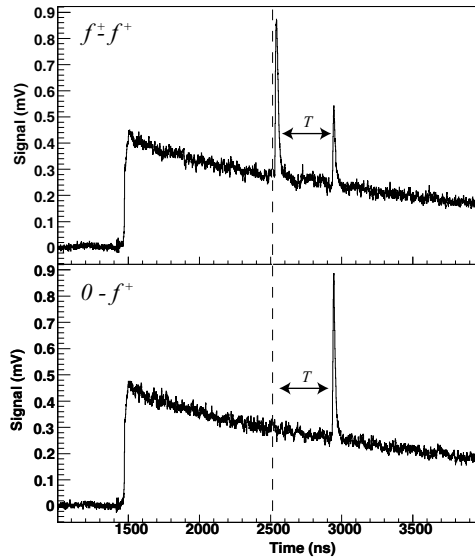


Figure 3: Laser stimulated annihilation peaks against the exponential decaying background of the other metastable states' populations. Mode 1): f^+-f^+ when both lasers are fired and mode 2): $0-f^+$ when only the second laser is fired. The peak in Mode 2) is larger than the second peak in Mode 1) because no previous depopulation of the state has been induced.

in figure 3. Mode 1) contained all the information about Γ_i while mode 2) was required to extract information about the refilling from higher states, also contained in 1).

The method employed in [13], [7] and [17] to determine the HF splitting included a microwave pulse between the first and second lasers of mode 1). By scanning the microwave over a range of frequencies and measuring the dependence of r_2 , the ν_{HF}^+ and ν_{HF}^- resonances were found. The maximum achievable signal for a range of laser delays was determined by fixing the microwave frequency to one transition, say ν_{HF}^+ , and monitoring r_2 while scanning the microwave power.

3. Apparatus

The experiment was performed at CERN's Antiproton Decelerator (AD), which delivered a pulse of $1-4 \times 10^7$ antiprotons with a length of 200 ns (FWHM) and an energy $E = 5.3$ MeV at ~ 90 s intervals. Antiprotonic helium was formed by stopping antiprotons in a gas target at a temperature of 6.1 K and a pressure $p = 150-500$ mbar (number density $1.7-6.2 \times 10^{20} \text{ cm}^{-3}$).

Charged pions were produced by antiproton annihilations in the helium nucleus and could be detected by Cherenkov counters. The signal was amplified by fine-mesh photomultipliers (PMTs) and the resulting analog delayed annihilation time spectrum (ADATS) was recorded in a digital oscilloscope (DSO). The PMTs were gated off during

the \bar{p} pulse arrival so that only the 3% metastable tail was recorded [21].

Two pulse-amplified laser beams were produced by splitting a continuous wave (cw) laser beam of wave-length 726.1 nm into two seed beams [7]. These were pulsed by amplifying the seeds using dye filled Bethune cells pumped by two pulsed Nd:Yag lasers, the second delayed by time T after the first. The pump beams were stretched so that the two pulse lengths were of the order ~ 15 ns [11] and therefore similar to the Auger decay rate ensuring a high depopulation efficiency. The maximum emitted energy fluence at the target was ~ 30 mJ/cm² with a spot diameter of 5 mm.

To measure the HF transitions, a microwave pulse was produced by a vector network analyzer (Anritsu 37225B) referenced to a 10 MHz GPS (HP 58503B) satellite signal and amplified by a pulsed travelling wave tube amplifier (TMD PTC6358). A cylindrical resonant microwave cavity with central frequency $\nu_0 = 12.91$ GHz provided the desired shape for the field (TM₁₁₀ mode) at the target. To cover the $\Delta\nu \sim 100$ MHz microwave scanning range, the cavity was over-coupled to the wave guide so that its loaded quality factor Q_L was ~ 100 , where $\Delta\nu = f_0/Q_L$ [22]. Most of the power was reflected back towards the amplifier and absorbed by an isolator. An antenna was connected to the cavity to monitor the field so that the desired power could be achieved by controlling the amplification of the pulse.

4. Analysis

4.1. Mode 1) ($f^+ - f^+$)

When both lasers were fired, the second delayed by a period T after the first, the normalized peak-to-total r_2/r_1 was plotted as a function of T . The data were fitted with a function derived from the integral of the following two equations:

$$\frac{d\rho_+}{dt} = g_+(t) - (\lambda_{+-} + \gamma_r)\rho_+ + \lambda_{-+}\rho_-, \quad (2a)$$

$$\frac{d\rho_-}{dt} = g_-(t) - (\lambda_{-+} + \gamma_r)\rho_- + \lambda_{+-}\rho_+, \quad (2b)$$

where ρ_{\pm} is the population density of the HF states, and $g_{\pm}(t)$ describes the refilling rate from the higher lying states. The relaxation rates from ρ_+ to ρ_- and ρ_- to ρ_+ are represented by λ_{+-} and λ_{-+} respectively. The radiative decay rate is $\gamma_r = 7.149 \times 10^5$ s⁻¹ [4], see figure 4.

If $t = 0$ is the time when the first laser is fired then the relative population of the two levels at $t < 0$ is

$$\rho_{\pm} = \frac{2F^{\pm} + 1}{2(2L + 1)}, \quad (3)$$

where $F^+ = L + \frac{1}{2}$ and $F^- = L - \frac{1}{2}$. The signal from the first and second laser are therefore

$$r_1 = I_0 \frac{L + 1}{2L + 1} \epsilon_1, \quad (4a)$$

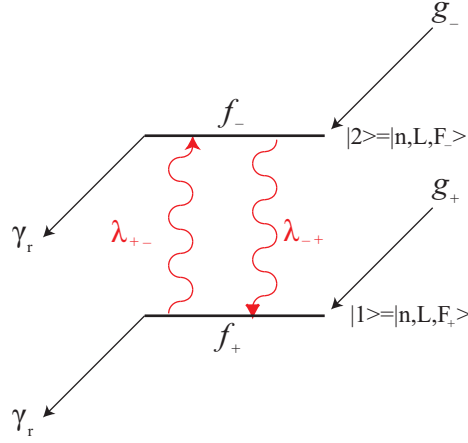


Figure 4: Energy level diagram of part of the cascade showing the refilling $g_{\pm}(t)$ from above states, decay to lower states γ_r and the relaxation collision rate $\lambda_{\pm\rightarrow\mp}$.

$$r_2(t) = I_0\rho_+(t)\epsilon_2, \quad (4b)$$

where I_0 is a normalization factor and ϵ_1 and ϵ_2 are the laser depopulation efficiencies for the first and second laser. The overlap of the laser peaks, whereby the F^- transition is partially induced due to the Doppler broadening when the laser is tuned to the f^+ transition, is considered negligible in this analysis.

At $t = 0$ and since $L \gg 1$, the initial populations are

$$\rho_+(0) = \frac{L+1}{2L+1}(1-\epsilon_1) \approx \frac{1}{2}(1-\epsilon_1), \quad (5a)$$

$$\rho_-(0) = \frac{L}{2L+1} \approx \frac{1}{2}. \quad (5b)$$

It can also be assumed that $\lambda_{+-} = \lambda_{-+} \equiv \Gamma_i$ and $g_+ = g_- \equiv g$. So (2a) and (2b) can be written as follows

$$\rho_+(t) = \frac{1}{2}e^{-\gamma_r t} \left(1 - \frac{\epsilon_1}{2} + \frac{\epsilon_1}{2}e^{-2\Gamma_i t} \right) + \frac{1}{2} \int_0^t e^{-\gamma_r(t-t')} \mu_f h(t') dt', \quad (6a)$$

$$\rho_-(t) = \frac{1}{2}e^{-\gamma_r t} \left(1 - \frac{\epsilon_1}{2} - \frac{\epsilon_1}{2}e^{-2\Gamma_i t} \right) + \frac{1}{2} \int_0^t e^{-\gamma_r(t-t')} \mu_f h(t') dt', \quad (6b)$$

where $g = \mu_f h(t)$, of which μ_f is a constant associated with the rate of filling from above states and $h(t)$ is the filling function normalized by $h(0) = 1$. The simplest assumption for $h(t)$ is $h(t) = e^{-\mu_0 t}$ where μ_0 is a decay rate associated with the population of the above states. This simplification was necessary to achieve an unambiguous result due to the limited amount of data. So the solution to the integral in (6a) and (6b) becomes

$$F(t) \equiv \mu_f \int_0^t e^{-\gamma_r(t-t')} h(t') dt' = \frac{\mu_f (e^{-\gamma_r t} - e^{-\mu_0 t})}{\mu_0 - \gamma_r}. \quad (7)$$

At $T < 1000$ ns the filling can be assumed constant $\mu_0 = 0$, and thus

$$F(t) = \frac{\mu_f(1 - e^{-\gamma_r t})}{\gamma_r}. \quad (8)$$

Substituting (8) into (6a), then (6a) into (4b) and normalizing over (4a) gives:

$$\frac{r_2(t)}{r_1(t)} = \frac{\epsilon_2}{\epsilon_1} \left[e^{-\gamma_r t} \left(1 - \frac{\epsilon_1}{2} - \frac{\epsilon_1}{2} e^{-2\Gamma_i t} - \frac{\mu_f}{\gamma_r} \right) + \frac{\mu_f}{\gamma_r} \right]. \quad (9)$$

4.2. Mode 2) (0- f^+)

Only firing the second laser, the population decay and refilling of the state can be measured. In this regime r_2 was normalized to the average r_1 from mode 1). This was performed so that both sets of data could be plotted on the same scale and compared adjacently. There are no inelastic collision terms because no asymmetry is created,

$$\frac{r_2(t)}{r_1(t)} = \frac{\epsilon_2}{\epsilon_1} \left[e^{-\gamma_r t} \left(1 - \frac{\mu_f}{\gamma_r} \right) + \frac{\mu_f}{\gamma_r} \right]. \quad (10)$$

4.3. Numerical simulation

The (37, 35) \rightarrow (38, 34) laser transition was numerically simulated by evolving the optical Bloch equations, obtaining a maximum depopulation efficiency of 70%.

The microwave transitions between the HF substates were determined by evolving (11a), derived from the optical Bloch equations, which can be written as two independent 4×4 matrices to handle the ν_{HF}^+ and ν_{HF}^- transitions separately. However, collision induced \bar{p} spin flips result in ν_{SHF}^+ and ν_{SHF}^- transitions. Thus the population evolutions of the J^{-+} and J^{++} states become dependent on those of the J^{--} and J^{-+} states. The resulting simultaneous equation has the solution of the form of an 8×8 matrix. An additional two dimensions were added to simulate the refilling from above states:

$$\frac{d}{dt} \boldsymbol{\rho} = \mathbf{M} \boldsymbol{\rho}, \quad (11a)$$

$$\boldsymbol{\rho} = \begin{pmatrix} \rho_{-+} \\ \rho_{++} \\ \rho_{x+} \\ \rho_{y+} \\ \rho_{--} \\ \rho_{+-} \\ \rho_{x-} \\ \rho_{y-} \\ \rho_{u38} \\ \rho_{u39} \end{pmatrix}, \quad (11b)$$

$$\mathbf{M} = \begin{pmatrix} -\gamma_c & \Gamma_i & 0 & \frac{1}{2}\Omega_m^+ & \Gamma_i & 0 & 0 & 0 & \gamma_{u38}/4 & 0 \\ \Gamma_i & -\gamma_c & 0 & -\frac{1}{2}\Omega_m^+ & 0 & \Gamma_i & 0 & 0 & \gamma_{u38}/4 & 0 \\ 0 & 0 & -\gamma_T & \Delta\omega_+ & 0 & 0 & 0 & 0 & 0 & 0 \\ -\Omega_m^+ & \Omega_m^+ & -\Delta\omega_+ & -\gamma_T & 0 & 0 & 0 & 0 & 0 & 0 \\ \Gamma_i & 0 & 0 & 0 & -\gamma_c & \Gamma_i & 0 & \frac{1}{2}\Omega_m^- & \gamma_{u38}/4 & 0 \\ 0 & \Gamma_i & 0 & 0 & \Gamma_i & -\gamma_c & 0 & -\frac{1}{2}\Omega_m^- & \gamma_{u38}/4 & 0 \\ 0 & 0 & 0 & 0 & 0 & 0 & -\gamma_T & \Delta\omega_- & 0 & 0 \\ 0 & 0 & 0 & 0 & -\Omega_m^- & \Omega_m^- & -\Delta\omega_- & -\gamma_T & 0 & 0 \\ 0 & 0 & 0 & 0 & 0 & 0 & 0 & 0 & -\gamma_{u38} & \gamma_{u39} \\ 0 & 0 & 0 & 0 & 0 & 0 & 0 & 0 & 0 & -\gamma_{u39} \end{pmatrix}, \quad (11c)$$

where $\rho_{-+}, \rho_{++}, \rho_{--}$, and ρ_{+-} represent the different time dependent populations of the four SHF states of the $(n, l) = (37, 35)$ state. In a field free region $\Omega_m = 0$, these populations simply decay radiatively at a rate of $\gamma_r = 7.149 \times 10^5 \text{ s}^{-1}$ to the $(36, 34)$ state and $0.0086 \times 10^5 \text{ s}^{-1}$ to the $(37, 34)$ state [4]. When there is a population asymmetry and an external oscillating magnetic field is present, transfer between the states can be observed. The complex dependency of the transitions is represented by $\rho_{x\pm}$ and $\rho_{y\pm}$ for the real and imaginary parts respectively. Broadening effects are dependent on both the radiative decay rate γ_r and the elastic collisional frequency Γ_e : $\gamma_T = \gamma_r + \Gamma_e$.

The four SHF states are refilled as the upper states, $(38,36)$ ρ_{u38} and $(39,37)$ ρ_{u39} , decay at a rate of $\gamma_{u38} = 6.55 \times 10^5 \text{ s}^{-1}$ and $\gamma_{u39} = 5.88 \times 10^5 \text{ s}^{-1}$ into the lower $(37, 35)$ state, as part of the cascade [4]. The initial populations of these states have been experimentally measured [18, 23]. Through inelastic relaxation collisions Γ_i the atoms return to an equilibrium, the variable γ_c is defined as $\gamma_c = 2\Gamma_i + \gamma_r$. Collisions which result in the spin flip of more than one particle are ignored [20].

The offset between the microwave frequency ν_M and transition frequencies $\nu_{\text{HF}\pm}$ is represented by $\Delta\omega = 2\pi(\nu_M - \nu_{\text{HF}\pm})$. The Rabi frequency is dependent upon the magnetic field strength B and the atom's magnetic dipole moment μ_m

$$\Omega_m = \frac{\mu_m B(x, y, t)}{\hbar}, \quad (12)$$

$$\mu_m = \langle n', L', F', J', m | \mu_M | n, L, F, J, m \rangle, \quad (13)$$

which can be calculated using Wigner's 3-j and Racah's 6-j coefficients

$$\begin{aligned} \langle n, L, F^-, J', m | \mu | n, L, F^+, J, m \rangle &= (-1)^{J'+m} \begin{pmatrix} J & 1 & J' \\ m & 0 & -m \end{pmatrix}_{3-j} \\ &\times \sqrt{(2J+1)(2J'+1)} \begin{Bmatrix} F^- & J' & \frac{1}{2} \\ J & F^+ & 1 \end{Bmatrix}_{6-j} \\ &\times \sqrt{(2F^++1)(2F^-+1)} \begin{Bmatrix} \frac{1}{2} & F^- & L \\ F^+ & \frac{1}{2} & 1 \end{Bmatrix}_{6-j} g_e \mu_b \langle \frac{1}{2} | s_e | \frac{1}{2} \rangle, \end{aligned} \quad (14)$$

where n, L, F, J, m are the corresponding quantum numbers.

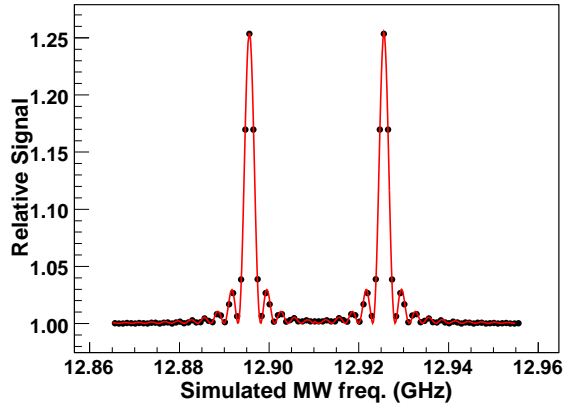


Figure 5: Simulated microwave resonance profile, where $T = 350$ ns $\Gamma_i = 3.4 \times 10^5$ s $^{-1}$, fitted with the same function as the experimental measurements presented in [7] and [17]

Equation (11a) was solved over a range of 60 equally spaced frequencies ν_M to simulate a microwave resonance profile measurement. The population positional distribution and magnetic field variance were modelled with a Monte Carlo positional simulation. The magnetic field distribution at the target is dependent on the cavity and varies spatially with respect to the radial r and angular cylindrical ϕ co-ordinates [22]. Apart from edge effects the cylindrical component z is constant. The radial B_r and angular B_ϕ components of the magnetic field are given by

$$B_r(r, \phi) = B_0 \frac{J_1(kr)}{kr} \sin(\phi), \quad (15a)$$

$$B_\phi(r, \phi) = B_0 J_1'(kr) \cos(\phi), \quad (15b)$$

where k is the wave number and J_1 is the Bessel function of the first kind. The stopping distribution of the $\bar{p}\text{He}^+$ is assumed to be Gaussian in both the z and r planes [22].

5. Results

Data were measured at three different target pressures $p = 150$ mbar, 250 mbar and 500 mbar resulting in a total of six graphs; three for mode 1) and three for mode 2). These were plotted side by side and fitted simultaneously with (9) and (10). The variables μ_f , ϵ_1 and Γ_i were common for all pressures, where the latter was weighted proportionally to the target gas density and ϵ_2 was left free for different target densities. Other, more complex fit functions were also attempted. These varied to include the population evolution of the upper levels and left ϵ_1 free for different target densities. However, the introduction of more parameters limited convergence and put emphasis on the refilling processes. It was found that the simplest function provided the most sensitivity to Γ_i .

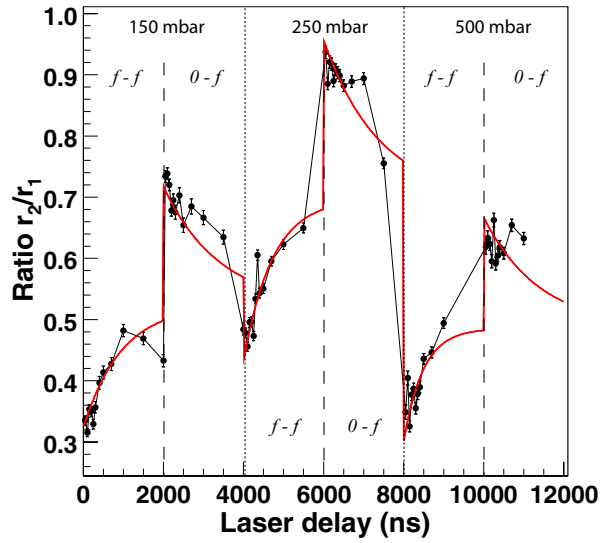


Figure 6: Simultaneous fitting of the data for $p = 150$ mbar, 250 mbar and 500 mbar. Mode 1) ($f^+ - f^+$) was fitted with (9) and mode 2) ($0 - f^+$) was fitted with (10). The refilling rate μ_f was a common parameter for all target densities and the laser depopulation efficiencies ϵ_1 and ϵ_2 were common parameters for different modes measured at the same density.

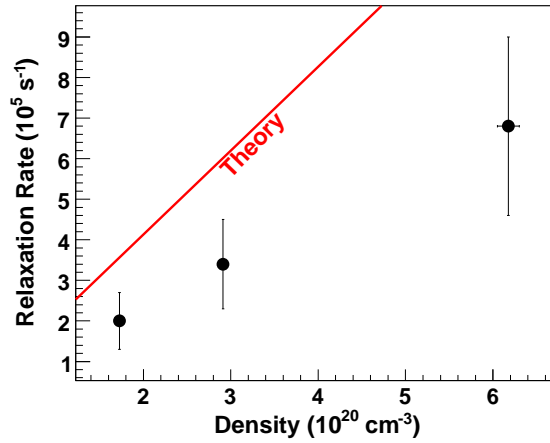


Figure 7: Dependence of the collision induced relaxation rate Γ_i on the helium target density.

A graph of the data fitted with (9) and (10) is shown in figure 6. The collision induced relaxation rate has been determined from the fitting parameters and plotted in figure 7. The numerical values are displayed in table 1 except for μ_f and ϵ_1 which were determined to be $(5.2 \pm 0.2) \times 10^5 \text{ s}^{-1}$ and 55% respectively.

The errors associated with these relaxation rates have been inflated by the square

Table 1:

p (mbar)	ρ_{He} (10^{20} cm^{-3})	ϵ_2 (%)	Γ_i (10^5 s^{-1})	τ_i (ns)
150	1.726	39(2)	2.0(0.7)	2500(900)
250	2.912	53(2)	3.4(1.1)	1500(500)
500	6.177	37(3)	6.8(2.2)	750(250)

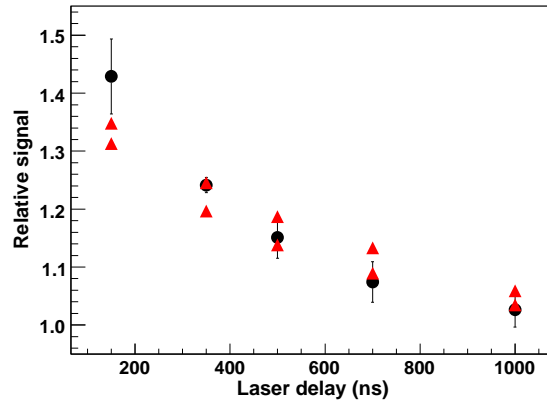


Figure 8: The optimum signal-to-noise ratio for each time delay T at $p = 250$ mbar. The circles (●) represent the experimental results from Pask *et. al.* [7] while the triangles (▲) represent the simulated data. The larger signal results from $\Gamma_i = 2.3 \times 10^5 \text{ s}^{-1}$ and the smaller from $\Gamma_i = 4.5 \times 10^5 \text{ s}^{-1}$

root of the reduced chi squared $\chi_{red}^2 \sim 10$ of the fit but still remain 2-3 sigma less than the most recent theoretical calculations which predict $\Gamma_i = 6.2 \times 10^5 \text{ s}^{-1}$ [24] for $p = 250$ mbar. The laser depopulation efficiency is also revealed to be smaller than the 70% predicted in Section 4.3. The fluctuations of ϵ_2 , that can vary by as much as 15%, are put down to the fact that data of different densities were measured on different days. The fluctuations are therefore most probably caused by changes in the overlap of the two lasers with the \bar{p} beam and each other.

To be certain that the fit provided a realistic determination of the collision parameter, microwave resonant scans were simulated as described in Section 4.3. The simulated signal-to-noise ratio for $T = 150$ ns, 350 ns, 500 ns, 700 ns and 1000 ns was compared to experimental data measured at $p = 250$ mbar from [7]. It was assumed that $\Gamma_e = 2.5\Gamma_i$ [20] and $\epsilon_1 = \epsilon_2 = 55\%$. The upper and lower limits, determined from the 1 sigma error associated with Γ_i , are plotted alongside the previously measured data, shown in figure 8.

At small T , $\Gamma_i = 4.5 \times 10^5 \text{ s}^{-1}$ tends to underestimate the signal-to-noise ratio while $\Gamma_i = 2.3 \times 10^5 \text{ s}^{-1}$ overestimates the signal when T is large. At $T = 200$ ns both the

upper and lower limits are too small. This is due to the laser depopulation efficiency, which has a larger effect on the signal at short T . The experimental data displayed in figure 8 were measured during a different year (2006) to those data displayed in figure 7 (2008). During this time the \bar{p} flux was larger with higher stability and therefore ϵ_1 and ϵ_2 were likely to be higher than during 2008.

6. Conclusions

This study of the collision rates between $\bar{p}\text{He}^+$ atoms and the He medium has been used both to determine optimal conditions for microwave resonance profile measurements and to compare with theoretical predictions so that the system may be better understood. Experimental measurements of elastic collisions published in previous papers [19] prompted a re-evaluation of theory [20] which had originally overestimated the collision rate. Since the cross-sections of the two collision processes were predicted to be similar, a measurement of the inelastic collision rate was expected to introduce valuable knowledge about the interactions.

For the first time inelastic spin exchange collisions have been measured between the HF states of $\bar{p}\text{He}^+$. Given the complexity of the system and the uncertainty in determining the initial parameters of the theoretical model, the measured values are in agreement with the recent theory [24]. More rigorous calculations are anticipated for a more thorough comparison.

The laser depopulation efficiency is shown to be smaller than predicted but also to depend heavily on the conditions of the \bar{p} beam and alignment. Simulations comparing the results to earlier data indicate agreement between the two methods but the inelastic collision rate is most likely to tend towards theory in the upper limits of experimental uncertainty.

Collisional effects in E1 transitions have previously been shown to vary depending on the state measured, therefore other states are of interest. A study of the collision processes in the $\bar{p}^3\text{He}^+$ HF structure, which contains an additional degree of freedom due to the helion spin, is also planned for future work.

Acknowledgments

The authors would like to acknowledge many fruitful discussions with Prof. Grigory Korenman (Moscow State University). We thank the AD operators for providing the antiproton beam. This work was supported by Monbukagakusho (grant no. 15002005), by the Hungarian National Research Foundation (NK67974 and K72172), the EURYI Award of the European Science Foundation and the Deutsche Forschungsgemeinschaft (DFG), the Munich-Centre for Advanced Photonics (MAP) Cluster of DFG and by the Austrian Federal Ministry of Science and Research.

References

- [1] R.S. Hayano, M. Hori, D. Horváth, and E. Widmann. Antiprotonic helium and CPT invariance. *Reports on Progress in Physics*, 70(12):1995–2065, 2007.
- [2] M. Iwasaki, S. N. Nakamura, K. Shigaki, Y. Shimizu, H. Tamura, T. Ishikawa, R. S. Hayano, E. Takada, E. Widmann, H. Outa, M. Aoki, P. Kitching, and T. Yamazaki. Discovery of antiproton trapping by long-lived metastable states in liquid helium. *Phys. Rev. Lett.*, 67:1246–1249, 1991.
- [3] T. Yamazaki, E. Widmann, R. S. Hayano, M. Iwasaki, S. N. Nakamura, K. Shigaki, F. J. Hartmann, H. Daniel, T. von Egidy, P. Hofmann, Y.-S. Kim, and J. Eades. Formation of long-lived gas-phase antiprotonic helium atoms and quenching by H₂. *Nature*, 361:238–240, 1993.
- [4] T. Yamazaki, N. Morita, R. S. Hayano, E. Widmann, and J. Eades. Antiprotonic helium. *Phys. Rep.*, 366:183–329, 2002.
- [5] G. T. Condo. On the absorption of negative pions by liquid helium. *Phys. Lett.*, 9:65, 1964.
- [6] D. Bakalov and V. I. Korobov. Hyperfine structure of antiprotonic helium energy levels. *Phys. Rev. A*, 57:1662–1667, 1998.
- [7] T. Pask, D. Barna, A. Dax, R.S. Hayano, M. Hori, D. Horváth, B. Juhász, C. Malbrunot, J. Marton, N. Ono, K. Suzuki, J. Zmeskal, and Widmann E. Improved Study of the Antiprotonic Helium Hyperfine Structure. *J. Phys. B: At. Mol. Opt. Phys*, 41(081008):081008, 2008.
- [8] H. A. Torii, R. S. Hayano, M. Hori, T. Ishikawa, N. Morita, M. Kumakura, I. Sugai, T. Yamazaki, B. Ketzer, F. J. Hartmann, T. von Egidy, R. Pohl, C. Maierl, D. Horváth, J. Eades, and E. Widmann. Laser measurements of the density shifts of resonance lines in antiprotonic helium atoms and stringent constraint on the antiproton charge and mass. *Phys. Rev. A*, 59:223–229, 1999.
- [9] M. Hori, J. Eades, E. Widmann, H. Yamaguchi, J. Sakaguchi, T. Ishikawa, R. S. Hayano, H. A. Torii, B. Juhász, D. Horváth, and T. Yamazaki. Sub-ppm laser spectroscopy of antiprotonic helium and a CPT-violation limit on the antiproton charge and mass. *Phys. Rev. Lett.*, 87:093401, 2001.
- [10] M. Hori, J. Eades, R. S. Hayano, T. Ishikawa, W. Pirkl, E. Widmann, H. Yamaguchi, H. A. Torii, B. Juhász, D. Horváth, and T. Yamazaki. Direct measurements of transition frequencies of isolated $\bar{\text{p}}\text{He}^+$ atoms, and new CPT violation limits on the antiproton charge and mass. *Phys. Rev. Lett.*, 91:123401, 2003.
- [11] M. Hori, A. Dax, J. Eades, K. Gomikawa, RS Hayano, N. Ono, W. Pirkl, E. Widmann, HA Torii, B. Juhász, et al. Determination of the antiproton-to-electron mass ratio by precision laser spectroscopy of $\bar{\text{p}}\text{He}^+$. *Phys. Rev. Lett.*, 96(24):243401, 2006.
- [12] E. Widmann, J. Eades, T. Yamazaki, H. A. Torii, R. S. Hayano, M. Hori, T. Ishikawa, M. Kumakura, N. Morita, I. Sugai, F.J. Hartmann, T. von Egidy, B. Ketzer, C. Maierl, R. Pohl, and D. Horváth. Hyperfine structure of the metastable $\bar{\text{p}}\text{He}^+$ atomcule revealed by a laser-induced $(n, l) = (37, 35) \rightarrow (38, 34)$ transition. *Phys. Lett. B*, 404:15–19, 1997.
- [13] E. Widmann, J. Eades, T. Ishikawa, J. Sakaguchi, T. Tasaki, H. Yamaguchi, R. S. Hayano, M. Hori, H.A. Torii, B. Juhász, D. Horváth, and T. Yamazaki. Hyperfine structure of antiprotonic helium revealed by a laser-microwave-laser resonance method. *Phys. Rev. Lett.*, 89:243402, 2002.
- [14] V. I. Korobov and D. Bakalov. Fine and hyperfine structure of the $(37,35)$ state of the $^4\text{He}^+\bar{\text{p}}$ atom. *J. Phys. B*, 34:L519, 2001.
- [15] N. Yamanaka, Y. Kino, H. Kudo, and M. Kamimura. Coupled rearrangement channel calculation of the fine and hyperfine structures of the antiprotonic helium atoms. *Phys. Rev. A*, 63:012518, 2000.
- [16] Y. Kino, N. Yamanaka, M. Kamimura, and H. Kudo. High precision calculation of the fine and hyperfine structure of antiprotonic helium-3,4 atoms. *Hyperfine Interactions*, 146-147:331–336, 2003.
- [17] T. Pask, D. Barna, A. Dax, S. Friedreich, R.S. Hayano, M. Hori, D. Horváth, B. Juhász,

- O. Massiczek, N. Ono, et al. Antiproton spin magnetic moment determined from the HFS of $\bar{p}\text{He}^+$. *Phys. Lett. B*, 678(1):0.
- [18] M. Hori, J. Eades, E. Widmann, H. Yamaguchi, J. Sakaguchi, T. Ishikawa, R. S. Hayano, H. A. Torii, B. Juhász, D. Horváth, and T. Yamazaki. Primary populations of metastable antiprotonic ^4He and ^3He atoms. *Phys. Rev. Lett.*, 89:093401, 2002.
- [19] Pask, T. Preliminary results from recent measurements of the antiprotonic helium hyperfine structure. *Hyperfine Interactions* - in press, 2009.
- [20] G. Ya. Korenman and S.N. Yudin. Coupled-channel analysis of collisional effects on hfs transitions in antiprotonic helium atoms. *J. Phys. B: At. Mol. Opt. Phys.*, 39:1473–1484, 2006.
- [21] M. Hori, K. Yamashita, R. S. Hayano, and T. Yamazaki. Analog cherenkov detectors used in laser spectroscopy experiments on antiprotonic helium. *Nucl. Instrum. Methods Phys. Res. A*, 496:102, 2003.
- [22] J. Sakaguchi, H. Gilg, R. S. Hayano, T. Ishikawa, K. Suzuki, E. Widmann, H. Yamaguchi, F. Caspers, J. Eades, M. Hori, D. Barna, D. Horváth, B. Juhász, H. A. Torii, and T. Yamazaki. Cryogenic tunable microwave cavity at 13 GHz for hyperfine spectroscopy of antiprotonic helium. *Nucl. Instrum. Methods Phys. Res. A*, 533:598–611, 2004.
- [23] M. Hori, J. Eades, E. Widmann, T. Yamazaki, R. S. Hayano, T. Ishikawa, H. A. Torii, T. von Egidy, F. J. Hartmann, B. Ketzer, C. Maierl, R. Pohl, M. Kumakura, N. Morita, D. Horváth, and I. Sugai. Populations and lifetimes in the $v = n - l - 1 = 2$ and 3 metastable cascades of $\bar{p}\text{He}^+$ measured by pulsed and continuous antiproton beams. *Phys. Rev. A*, 70:012504, 2004.
- [24] Korenman, G.Y. and Yudin, SN. Collisional effects on hfs transitions of antiprotonic helium. *Hyperfine Interactions* - in press, 2009.